Fundamentals of Solar-Sail Transfers Around Planetary Bodies

Gámez Losada, F.; Visser, P.N.A.M.; Heiligers, M.J.

Important note
To cite this publication, please use the final published version (if applicable).
Please check the document version above.

Fundamentals of Solar-Sail Transfers Around Planetary Bodies

Fernando Gámez Losada[(1)], Pieter Visser[(2)], Jeannette Heiligers[(3)]

Affiliation (all): Faculty of Aerospace Engineering, Delft University of Technology
City, Country: Delft, The Netherlands
Email: [(1)] F.GamezLosada@tudelft.nl, [(2)] P.N.A.M.Visser@tudelft.nl, and [(3)] M.J.Heiligers@tudelft.nl

The problem of how to solar sail around planets remains nearly unexplored. Most of the existing body of knowledge focuses on scape trajectories or locally optimal controls, not providing much insight into the inherent physical characteristics of the transfer problem. In this work, we present the first comprehensive study of solar-sail transfers around planetary bodies by analysing the simplest conceivable transfer, the planar Circular-to-Circular (C2C) transfer. The C2C transfer spans for only one orbital revolution, constituting the building block of more complex multi-revolution trajectories. By patching together a series of C2C transfers, a feasible initial guess for trajectory optimisation algorithms can be generated. The optimised control law maximises the orbital radius within the C2C transfer. The radius change is used as performance metric. The results suggest that the domain of the control variables can be substantially reduced, effectively enhancing convergence of the optimal control solver, and significantly reducing computational time. Furthermore, a dimensional analysis shows that the C2C performance only depends on one parameter: the ratio of the sail's characteristic acceleration over the local gravitational acceleration. The scaled nature of the results allows to easily compute the C2C performance for a wide range of mission scenarios around any planetary body, providing a new tool for early mission design.

I. INTRODUCTION

A solar sail is a large, thin, mirror-like surface deployed in space and held in place by centrifugal force or by a lightweight structure. Its principle of operation is simple: reflecting sunlight. Although massless, photons carry momentum. When reflected, they impinge a force upon the sail, yielding a measurable and controllable thrust of the order of magnitude of a small ion drive (for near term solar-sail technology). A solar sail's main advantage: it does not require propellant. The only limitation on the lifespan of a solar sail is the degradation of the sail's film in the harsh space environment [1].

The body of knowledge of solar-sail trajectory optimization mainly focuses on heliocentric trajectories (started by works like [2] [3]). Planet-centred trajectories have been investigated to a much lesser extent, potentially due to the greater complexity of the problem. However, solar-sail technology will mature right here, around our home planet. We therefore believe in the importance of understanding the basics of solar sailing around planets, as Earth-centred sailing will be the cradle of future interplanetary missions.

Previous research on optimising solar-sail trajectories around Earth focused on (blended) locally optimal control laws [4] [5] and often considered open-ended trajectories instead of orbital transfers [6] [7]. The very few works that do consider orbital rendezvous trajectories based on optimal control theory [8] [9] consider specific cases (e.g., from the geostationary orbit to the graveyard orbit), leaving insight into the general problem unexplored.

In this paper, we present the first comprehensive study of solar-sail transfer trajectories around planetary bodies by investigating the simplest form of transfer trajectory: the planar Circular-to-Circular orbit transfer (C2C). The objective of the C2C transfer is defined as maximising the orbital radius within one orbital revolution, starting from, and ending in planar circular orbits. The C2C transfer could be viewed as the equivalent of the Hohmann transfer for solar sails. By understanding the basics of the C2C transfer, a foundation is laid upon which – in future research – more complex multi-revolution trajectories can be computed efficiently. For example, by patching together a series of one-revolution C2C transfers, a feasible initial guess for a many-revolutions trajectory optimisation algorithm can be assembled.

The remainder of this paper is organised as follows: Section II poses the optimisation problem behind the C2C transfer as well as the Equations of Motion (EoM) of the solar sail. Section III analyses the performance of the C2C transfer as a function of the Sun-orbit geometry and the ratio of the sail's characteristic acceleration over the local gravitational acceleration. Section IV elaborates on the control laws required to execute the C2C transfer and shows the various regimes that exist for the C2C transfer. Section V highlights some possible applications of this work. Finally, Section VI gathers the conclusions drawn from this study.

II. OPTIMISATION PROBLEM

The C2C transfers presented in this paper arise as the solution of the following optimisation problem:

$$\max_{\boldsymbol{u} \in U}\{r(t_f)\} \; s.t. \, EoM \; \& \; e(t_f) = 0, \qquad (1)$$

where $\boldsymbol{u}$ is the control vector, U the set of admissible controls (see Section IV), r the orbital radius, EoM the Equations of Motion with associated initial conditions (see Section II.A for the complete formulation), e the osculating eccentricity, and t_f the final time. The C2C transfer is defined as to span for one orbital revolution, meaning that, at t_f, the initial and final position vectors are parallel. Due to the small magnitude of the solar-sail acceleration, the radius increase will be small, and the final time will be approximately equal to the initial orbital period.

The optimisation problem in (1) is solved using the commercially available GPOPS-II software. GPOPS-II uses direct collocation (i.e., variable-order Gaussian quadrature methods) to translate the continuous optimal control problem into a non-linear program that is then solved with IPOPT [10].

A. Equations of motion

In this study, the motion of the solar sail around a planet is described in an inertial reference frame using point gravity and the ideal solar-sail model [1]. The EoM adopt the form:

$$\frac{d\boldsymbol{r}}{dt} = \boldsymbol{v}; \qquad \frac{d\boldsymbol{v}}{dt} = -\frac{\mu}{r^3}\boldsymbol{r} + a_0 \left(\widehat{\boldsymbol{S}} \cdot \widehat{\boldsymbol{n}}\right)^2 \widehat{\boldsymbol{n}}, \qquad (2)$$

Where $\boldsymbol{r}$ is the position vector, $\boldsymbol{v}$ the velocity vector, t the independent variable time, μ the planet's gravitational constant, a_0 the sail's characteristic acceleration at the planet's average distance from the Sun, $\widehat{\boldsymbol{S}}$ the direction of the Sunline, and $\widehat{\boldsymbol{n}}$ the normal vector perpendicular to one of the sail's surfaces. Numerical integration of (2) with the initial state $(\boldsymbol{r_0}, \boldsymbol{v_0})$ at $t = 0$ and the control law $\widehat{\boldsymbol{n}} = \widehat{\boldsymbol{n}}(t)$ provides the trajectory of the solar sail $(\boldsymbol{r} = \boldsymbol{r}(t), \boldsymbol{v} = \boldsymbol{v}(t))$ around the planet.
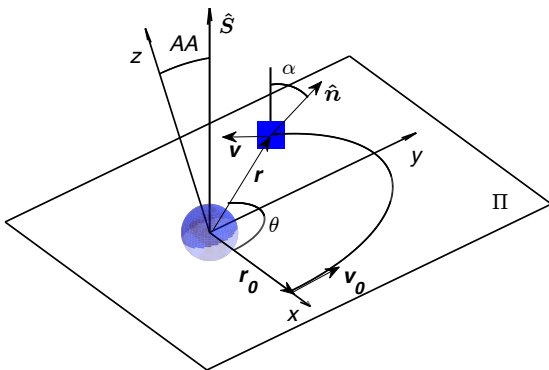

Fig. 1. Schematic of the reference frame, vectors, and important angles involved in the formulation of the Equations of Motion.

Fig. 1 depicts a schematic of the reference frame, vectors, and important angles involved in the formulation of the EoM. The inertial reference frame $C(x, y, z)$ is centred at the planet. The x-axis results from the cross product of the direction of the Sunline $\widehat{\boldsymbol{S}}$ and the orbit's angular momentum vector $\boldsymbol{h} = \boldsymbol{r_0} \times \boldsymbol{v_0}$. The z-axis is aligned with $\boldsymbol{h}$ and the y-axis lies in the orbital plane completing the right-handed triad. The Aspect Angle (AA) is the angle between the Sunline and $\boldsymbol{h}$. It determines the illumination conditions of the orbital plane: for $AA = 0$ deg and $AA = 90$ deg the orbit is perpendicular and parallel to the incoming sunlight, respectively. The cone angle α is the angle between $\widehat{\boldsymbol{n}}$ and $\widehat{\boldsymbol{S}}$. It determines the illumination conditions of the solar sail and thus its performance: $\alpha = 0$ deg and $\alpha = 90$ deg create a maximum and zero solar-sail acceleration (SSA), respectively. For the remainder of the paper, it is important to mention that $\tilde{\alpha} = 35.26$ deg is the cone angle that maximises the in-plane projection of the SSA when $AA = 0$ deg [1]. The argument of latitude θ is the angle between $\boldsymbol{r}$ and the x-axis. In this study, $\boldsymbol{r_0}$ is always aligned with the x-axis and $\boldsymbol{v_0}$ with the y-axis (see Fig. 1). Consequently, in a C2C transfer, $\theta \in [0, 2\pi]$.

The Sun is assumed to be infinitely far away from the planet (i.e., sunlight parallel to $\widehat{\boldsymbol{S}}$). In addition, we neglect the motion of the Sun as viewed from the planet, because the transfer time is significantly shorter than the orbital period of the Sun around the planet.

The C2C transfer is assumed to be two-dimensional (2D) and remains in the initial orbital plane Π defined by $\boldsymbol{h}$. The out-of-plane component of the SSA (i.e., $a_0 \left(\widehat{\boldsymbol{n}} \cdot \widehat{\boldsymbol{S}}\right)^2 \widehat{\boldsymbol{n}} \cdot \widehat{\boldsymbol{z}}$) is therefore neglected; only the in-plane SSA is considered in the EoM. Note that the small magnitude of the SSA and the periodicity of the control for a C2C transfer cause a negligible out-of-plane motion during the transfer.

To improve numerical stability during the optimisation, the EoM are scaled using the initial position, velocity, and orbital period $T_0 = 2\pi\sqrt{r_0^3/\mu}$, yielding:

$$\frac{d\boldsymbol{\rho}}{d\tau} = 2\pi\boldsymbol{\xi}; \qquad \frac{d\boldsymbol{\xi}}{d\tau} = 2\pi\left[-\frac{\boldsymbol{\rho}}{\rho^3} + \Psi\boldsymbol{u}\right], \qquad (3)$$

where $\boldsymbol{\rho} = \boldsymbol{r}/r_0$, $\boldsymbol{\xi} = \boldsymbol{v}/v_0$, $\tau = t/T_0$, $\boldsymbol{u} = \left(\widehat{\boldsymbol{S}} \cdot \widehat{\boldsymbol{n}}\right)^2 \widehat{\boldsymbol{n}}$, and $\Psi = a_0/g_0$. $g_0 = \mu/r_0^2$ is the local gravitational acceleration at the initial state.

The scaled EoM only depend on one dimensionless parameter, the scaled characteristic acceleration Ψ. Ψ represents the "strength" of the sail relative to the local gravity. A particular sail design around a planet will yield a smaller value for Ψ the closer it gets to the planet. Note that two real problems (e.g., initial circular orbits around Mars and Earth) with the same scaled initial conditions, control $\boldsymbol{u} = \boldsymbol{u}(\tau)$ and Ψ yield the same scaled trajectory. By studying the scaled C2C transfers as a function of the parameter Ψ, we can later extrapolate the results to a wide range of real mission scenarios (see Section III).

Given $\widehat{\boldsymbol{S}}$, we can easily compute the control law $\widehat{\boldsymbol{n}} =$

$\widehat{\boldsymbol{n}}(t)$ (e.g., expressed through two attitude angles) from the control vector $\boldsymbol{u} = \boldsymbol{u}(t)$. In our analyses, we use $\boldsymbol{u}$ instead of $\widehat{\boldsymbol{n}}$ as it provides a more intuitive understanding of the thrusting capabilities of a solar sail (see Section II.B). Note that $\boldsymbol{u} = [u_x, u_y, u_z]$ is the SSA scaled with a_0.

B. Set of admissible controls
The control set B contains all possible control vectors that can be generated by an ideal solar sail:

$$B = \left\{ \boldsymbol{u} = \left(\widehat{\boldsymbol{S}} \cdot \widehat{\boldsymbol{n}}\right)^2 \widehat{\boldsymbol{n}} : \widehat{\boldsymbol{n}} \cdot \widehat{\boldsymbol{S}} > 0 \right\}. \qquad (4)$$

B is commonly represented with the "bubble" surface diagram. As an example, Fig. 2 shows the (hollow) bubble diagram in frame C for $AA = 0$ deg (i.e., the Sun is along the negative z-axis). The projection of the bubble diagram onto the orbital plane generates the 2D set B_Π. B_Π represents the control at our disposal for in-plane manoeuvres. An equivalent projection could be defined for out-of-plane manoeuvres. However, as mentioned above, in this work we neglect the out-of-plane component of the SSA and thus focus only on B_Π; the out-of-plane projection can be viewed as wasted control.
Note that the bubble diagram of a spacecraft equipped with an ion drive is not a hollow bubble, but a solid sphere: the control vector can be pointed anywhere in inertial space and modulated between zero and the maximum available thrust. As the spacecraft consumes propellant, the sphere grows, reaching its maximum size at the end of the mission.
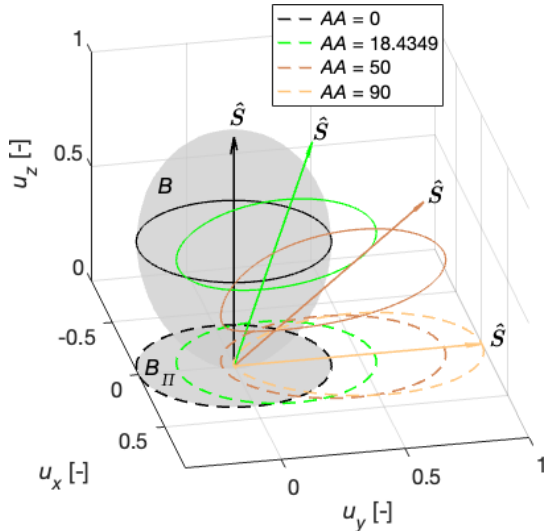

Fig. 2. Depiction of the various control sets as a function of the AA. Solid lines represent U, dashed lines U_Π.

For a zero aspect angle, $AA = 0$ deg, an ion drive would produce an equivalent B_Π as a solar sail (i.e., a circle, see Fig. 2) but with no out-of-plane waste. However, for $AA = 90$ deg, the resulting B_Π for a solar sail differs completely from that of an ion drive (i.e., still a circle). Hence, it is expected that, for $AA = 0$ deg, the computed solar-sail transfers will closely resemble that of ion-drive transfers, whereas for $AA = 90$ deg, the resulting transfers will be entirely different.
Set B can be constrained from the "bubble" surface to a line by applying Pontryagin's maximum principle. The maximum principle states that, to obtain an optimal trajectory, the controls $\boldsymbol{u}$ must minimise the Hamiltonian H throughout the entire trajectory, always adopting values within the so-called admissible controls [2] (for an ideal solar sail, the set of admissible controls is B). Mathematically:

$$\min_{\boldsymbol{u} \in B} \{ H = r_f + \boldsymbol{\lambda}_r \cdot \boldsymbol{v} + \boldsymbol{\lambda}_v \cdot (\boldsymbol{g} + a_0 \boldsymbol{u}) \}, \qquad (5)$$

where $\boldsymbol{g}$ is the gravitational acceleration, and $\boldsymbol{\lambda}_r$ and $\boldsymbol{\lambda}_v$ are the position and velocity co-states, respectively. Note that the part of H that explicitly depends on $\boldsymbol{u}$ is $H = \boldsymbol{\lambda}_v \cdot \boldsymbol{u}$. Then, Pontryagin's principle reduces to:

$$\max_{\boldsymbol{u} \in B} \{ \widehat{\boldsymbol{q}} \cdot \boldsymbol{u} \}, \qquad (6)$$

where $\widehat{\boldsymbol{q}} = -\boldsymbol{\lambda}_v / \lambda_v$ is the so-called primer vector direction. Equation (6) indicates that, to attain an optimal solution, we must orient the sail so that the projection of the control vector along the primer vector direction is maximised. We do not know a priori the evolution of the primer vector direction, but we know that it is contained in the orbital plane Π. In [1], McInnes solves the optimisation problem in (6), providing an explicit equation (see Section IV.A, (11)) to compute the optimal $\boldsymbol{u}$ for any given $\widehat{\boldsymbol{q}}$. Thus, we can compute all $\boldsymbol{u}$ vectors for all possible $\widehat{\boldsymbol{q}}$ vectors in Π to obtain a reduced set of admissible controls:

$$U = \left\{ \boldsymbol{u} = \arg\max_{\boldsymbol{u} \in B} [\widehat{\boldsymbol{q}} \cdot \boldsymbol{u}] : \widehat{\boldsymbol{q}} \in \Pi \right\}. \qquad (7)$$

Fig. 2 shows the reduced set of admissible controls U in frame C for increasing values of the AA (solid lines). As with B, the projection of U onto Π (i.e., U_Π) reveals the available control for in-plane manoeuvrers (dashed lines). The projected curves U_Π match the contours of B_Π (as an example, see the black curve and the grey surface for $AA = 0$ deg in Fig. 2), as they represent the maximum available in-plane control for each AA. This result is somewhat intuitive. To achieve a maximum radius solution, the control (i.e., in-plane thrust) must be maximised at every time-step. Indeed, any optimisation problem that can be interpreted as a minimum time problem (e.g., fastest orbit raising, fastest C2C transfer) will employ a control law in U.
U can be used to restrict the domain of the control variables to speed up the optimisation. One no longer has to consider all possible orientations in B, but only the subset in U. Even more, U can be used to reduce the number of control variables by substituting the control

vector $\boldsymbol{u}$ with the primer vector $\hat{\boldsymbol{q}}$. Because $\boldsymbol{u}$ can be expressed as a function of $\hat{\boldsymbol{q}}$, it is sufficient to use one angle to locate $\hat{\boldsymbol{q}}$ in the orbital plane rather than using two angles to define the orientation of $\boldsymbol{u}$ in 3D space. In this study, the angle δ between the y-axis and the primer vector $\hat{\boldsymbol{q}}$ was used as the control variable (see Fig. 3). Note that, for conventional unconstrained propulsion systems (e.g., chemical propulsion, ion drives), there would be no advantage in replacing $\boldsymbol{u}$ with $\hat{\boldsymbol{q}}$, since $\boldsymbol{u}$ can be aligned with $\hat{\boldsymbol{q}}$.

A more intuitive approach to defining the control variable would be to use the yaw angle A of the control and U_Π. Fig. 1 shows a schematic of the solar sail at an epoch mid-transfer. Fig. 3 shows the available in-plane control U_Π in frame C at that epoch as well as the velocity vector $\boldsymbol{v}$. The yaw angle A defines the direction of the in-plane projection of the control vector $\boldsymbol{u}_\Pi$ with respect to this instantaneous velocity vector. It determines how the control is distributed among the along-track, radial and cross-track directions. The magnitude of the control is also defined by the yaw angle, as the endpoint of the control vector must lie on U to obtain an optimal solution. Once U is defined, we thus only need the yaw angle to compute optimal in-plane manoeuvres. However, since an explicit mathematical relation between $\boldsymbol{u}$ in U and the yaw angle could not be found, the primer vector formulation was used instead.
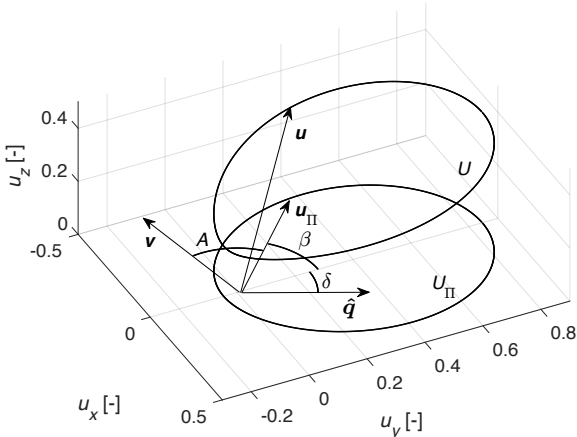

Fig. 3. Schematic of set U with a control vector $\boldsymbol{u}$ and relevant control angles.

III. PERFORMANCE

The performance of the C2C transfer is defined as the achieved radius increase after one orbital revolution scaled with the initial radius:

$$\eta = \frac{\delta r}{r_0}. \qquad (8)$$

In this section, we analyse the dependency of η on the scaled characteristic acceleration Ψ and the aspect angle AA.

Fig. 4 shows the performance η as a function of the orbit aspect angle AA for several values of Ψ. The values for η are scaled with the minimum performance at $AA = 90$ deg, η_{90}, so that all cases have a minimum performance of one. Two significant conclusions can be drawn from Fig. 4:

1) The best performance is achieved for $AA = 0$ deg (i.e., the incoming sunlight is perpendicular to the orbital plane), and the minimum performance for $AA = 90$ deg (i.e., the incoming sunlight is parallel to the orbital plane). The difference is a factor of 20. Performance thus drops significantly as the aspect angle increases. Compare, for example, a solar-sail debris removal mission in the LEO and GEO regions, where the debris is transferred from a circular initial orbit to a higher-altitude circular graveyard orbit, respectively. The AA of most objects in LEO is in the range $[0, 60]$ whereas for the GEO belt the aspect angle oscillates between $[67, 90]$ deg. Based on the results in Fig. 4, it can immediately be concluded that a solar sail would be much more effective for such a mission in LEO than in GEO. It is interesting to note that, for pure orbit raising (i.e., no eccentricity control), the best geometry occurs for $AA = 90$ deg.

2) The shape of the scaled performance curve seems similar for different Ψ values. Based on this observation, we assume that the dependency of η on aspect angle and scaled characteristic acceleration is separable and can be formulated as:

$$\eta = \eta_r(\Psi)\,\chi(AA), \qquad (9)$$

where η_r is a reference performance value obtained for a particular AA that only depends on Ψ, and χ is the shape function, which maps η_r to different AA values. Fig. 4 thus shows $\chi(AA)$ for $\eta_r = \eta_{90}$.
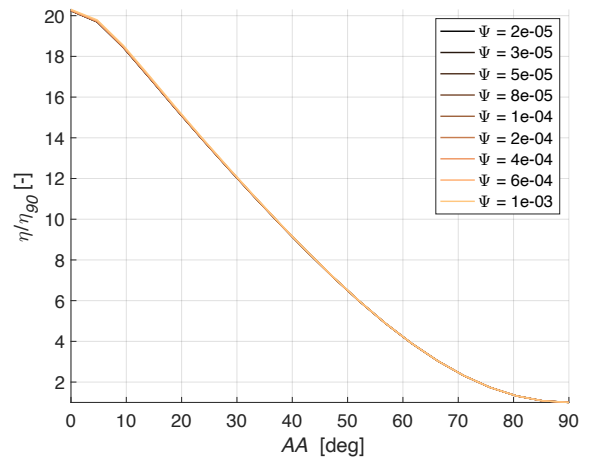

Fig. 4. Scaled performance over AA for various values of Ψ.

Fig. 5 shows three selected values of η_r as a function of the scaled characteristic acceleration Ψ: maximum

performance at $AA = 0$ deg ($\eta_r = \eta_0$), performance at $AA = 40$ deg ($\eta_r = \eta_{40}$), and minimum performance at $AA = 90$ deg ($\eta_r = \eta_{90}$). The figure indicates that η_r increases for increasing values of Ψ. In other words, as the initial altitude increases, the local gravitational acceleration decreases and thus the effect of the solar sail on the trajectory increases, yielding a larger δr. Note that, when using the same sail around the same planet, increasing values of Ψ correspond to increasing initial altitudes.

Hereinafter, we choose η_{40} as the reference performance value η_r in (9).

There seems to be a clear linear relation between η_r and Ψ in log-log scale. Consequently, we furthermore assume that:

$$\eta_r = n\Psi^m, \qquad (10)$$

where n and m are coefficients obtained by linear regression of the data points shown in Fig. 5. The values for n and m for $\eta_r = \eta_{40}$ are: $n = 2.19795377$, and $m = 1.00062885$.

By adequately using Fig. 4 and Fig. 5, one can readily obtain an estimate of the initial transfer performance of a particular mission scenario. For example, consider a solar sail with sail loading $\sigma = 0.18$ kg/m^2 at Venus in an orbit with $r_0 = 18,000$ km and an aspect angle of $AA = 30$ deg. This scenario yields a value for Ψ of 1×10^{-4}. Entering Fig. 5, we find that the reference performance η_{40} for $\Psi = 1 \times 10^{-4}$ is approximately 2×10^{-4}. Then, using Fig. 4 and (9), we obtain $\eta_{30} = \eta_{40}\,\chi_{30}/\chi_{40} = 2 \times 10^{-4} \times 12/9 = 2.7 \times 10^{-4}$.

Finally, from (8) we obtain that the achievable increase in radius after one orbital revolution is $r_0\,\eta_{30} = 4.8$ km. Note that the presented workflow is valid for any planet orbiting a star. One just has to substitute the correct physical parameters to compute Ψ, know the aspect angle of the orbit and δr is readily available. However, the linearity shown in Fig. 5 breaks down at large Ψ values. At sufficiently large Ψ values, the solar sail is blown away from the planetary system before it completes the C2C transfer, because the gravity of the planet is too small to balance the SSA. It is found that for Ψ below 1×10^{-2}, (10) and Fig. 5 remain valid.
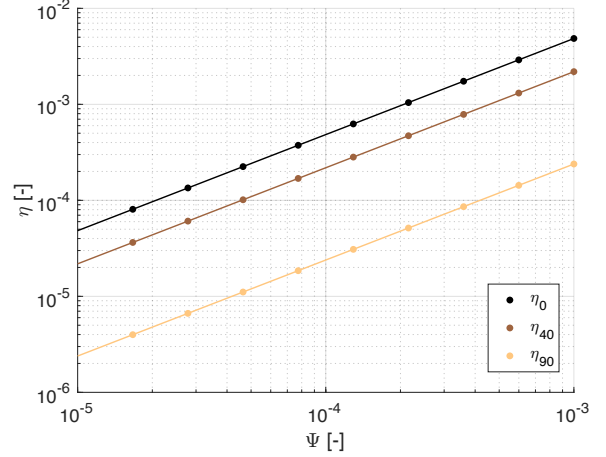

Fig. 5. Reference performance values for $AA = 0$, $AA = 40$, and $AA = 90$ deg as a function of Ψ.

IV. CONTROL

Fig. 6 shows the set of admissible controls U_Π (thin lines) together with the controls that are actually used in the C2C transfer (solid circular markers) for increasing aspect angles, where lighter colours represent larger aspect angles. Note that the thin lines in Fig. 6 are the same as the dashed lines in Fig. 2. We define the inner angle β as the angle between the y-axis and the projection of the control vectors in the orbital plane $\boldsymbol{u}_\Pi$ (see Fig. 3). This inner angle is the in-plane equivalent of the cone angle. In fact, for $AA = 90$ deg, the cone angle and inner angle are equal. The following important facts can be observed in the figure:

1) There is a critical value of the AA for which the computed control no longer traverses the whole available set of U_Π but is confined to a specific region around the origin. We refer to this AA as the critical aspect angle (AA_c) (see Section IV.A for more details). Note that the light-green contour in the figure is the set U_Π associated with AA_c. It is as if above AA_c, the computed control bounces off an invisible (y, z)-plane rotated around the z-axis by a critical inner angle β_c and is no longer able to access the remaining U_Π. We refer to this plane as the boundary plane. From Fig. 6, the boundary plane is defined as the (y, z)-plane that cuts the U set for the critical aspect angle (i.e., the green contour in Fig. 6) at the "hinge points". The hinge points are the two points in U with cone angle $\tilde{\alpha}$.

2) Only at the critical aspect angle does the control reach the boundary plane. For larger aspect angles, the control does not extend fully up to the boundary plane. Even so, we can use the concept of the boundary plane to further restrict the set of accessible controls U for $AA > AA_c$. Indeed, the boundary plane effectively restricts the sail cone angle to a specific cone angle band (see Section IV.B for an in-depth explanation).
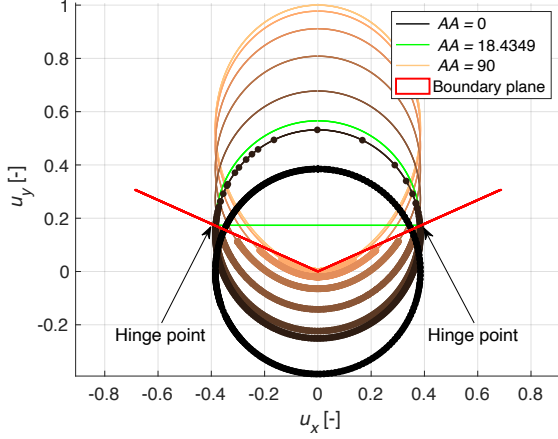
Fig. 6. U_Π projections for increasing AA (thin lines) together with the computed controls (solid circular markers).

A. Critical geometry

This subsection will explore the geometry at the critical aspect angle to gain a further understanding of the concept and to allow an analytical solution for the value for AA_c.

Fig. 7 represents the main geometrical dimensions of U as a function of the aspect angle: for each AA, the maximum (solid lines) and minimum (dashed lines) values of u_x, u_y and u_z for all control vectors in U are displayed. Note that the geometry of U_Π is given by u_y and u_x. The critical AA occurs when $u_{y,max} = u_{z,max}$ (green vertical line in Fig. 7), i.e., when the maximum out-of-plane dimension of U is the same as the maximum in-plane dimension. Why this condition results in the critical aspect angle is yet unknown but will be part of future investigations.
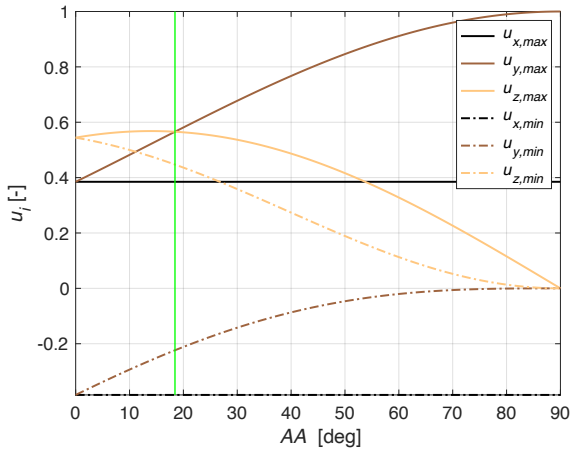

Fig. 7. Evolution of the characteristic dimensions of U with AA.

The critical aspect angle AA_c can be computed analytically. To do so, we make use of the angles and vectors displayed in the schematic in Fig. 8. Note that the depicted vector $\boldsymbol{u}$ yields the largest projection along

the y-axis among all possible $\boldsymbol{u} \in U_c$. For $u_{y,max} = u_{z,max}$ to be true, the angle between $\boldsymbol{u}$ and the y-axis must be $\pi/4$. From Fig. 8, $\varphi - \alpha^* = \pi/4$, where α^* is the cone angle of the vector $\boldsymbol{u}$ and φ is the angle between the y-axis and $\hat{\boldsymbol{S}}$. McInnes [1] shows that α^* is related to φ via:

$$\alpha^* = \frac{1}{2}\left[\varphi - \sin^{-1}\left(\frac{\sin\varphi}{3}\right)\right]. \qquad (11)$$

Substituting $\alpha^* = \varphi - \pi/4$ into (11) and solving for φ yields: $\varphi = 2\tan^{-1}\left[1\backslash3(\sqrt{10} - 1)\right]$. Finally, from Fig. 8, the critical aspect angle can be computed as $AA_c = \pi/2 - \varphi = 18.43$ deg.

The AA_c is geometrically linked with the critical inner angle β_c, which defines the orientation of the boundary plane represented in Fig. 6. β_c is the inner angle of the vector $\boldsymbol{u} \in U_c$ with cone angle $\tilde{\alpha}$. From the critical geometry: $\beta_c = \tan^{-1}(\sin\tilde{\alpha}/(\cos\tilde{\alpha}\,\sin AA_c)) = 65.91$ deg.
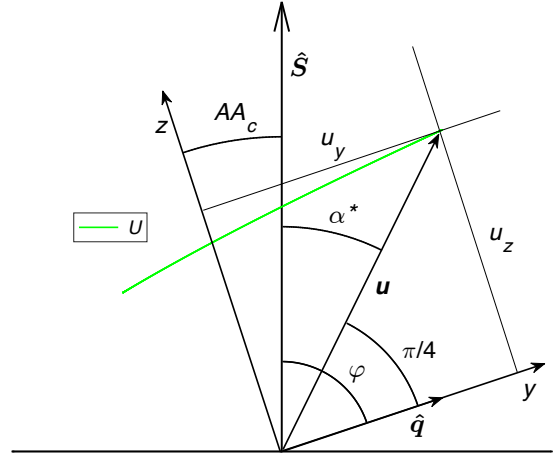

Fig. 8. Schematic of the critical geometry.

B. Cone angle bands

This section investigates whether the set of admissible controls U can be even further restricted. To that end, the relation between the aspect angle, the cone angle and the inner angle is explored with the aim of defining so-called "cone angle bands". These bands help in limiting the search space for an optimal control solver. An additional result is the identification of three distinct C2C transfer regimes, characterised by the value of the aspect angle.

Fig. 9 shows the cone angle as a function of the inner angle for various AA, where lighter colour indicates larger aspect angles. The solid circular markers represent the optimal controls computed using GPOPS-II. For $AA = 0$ deg, the cone angle is $\tilde{\alpha} = 36.26$ deg for all inner angles, whereas for $AA = 90$ deg, the inner angle matches the cone angle. The highlighted green line corresponds to the critical set U_C for $AA = 18.48$ deg.

The vertical red line denotes the boundary plane. Note that Fig. 9 is just a different representation of Fig. 6. Depending on the value for AA, different C2C transfer regimes can be defined:

1) *Ion drive* $(0 \leq AA < AA_c)$ regime: The solar sail behaves like an ion drive. The control is unrestricted and uses the totality of the admissible controls U. For $0 < AA < AA_c$, the cone angle of the computed controls oscillates above and below $\tilde{\alpha}$ (see the solid circular markers to the left of the boundary plane in Fig. 6).

2) *Critical* regime $(AA = AA_c)$: The control no longer accesses the region with $\alpha < \tilde{\alpha}$. The computed control bounces off the boundary plane, which acts as an invisible barrier that cannot be trespassed for $AA > AA_c$ (see how the solid circular markers keep to the right of the boundary plane in Fig. 6). At the critical aspect angle, the exact cone angle limits of the employed control can be computed: the minimum cone angle is $\tilde{\alpha}$ and the maximum cone angle is that of U. Note that (11) can be used to compute the minimum and maximum cone angles of U. From Fig. 8 one can infer that $\varphi_{min} = \pi/2 - AA$ and $\varphi_{max} = \pi/2 + AA$. Substitution of these values in (11) gives the min/max cone angles as a function of AA. Thus, at the critical aspect angle, the maximum cone angle is that of U and equals 45 deg.
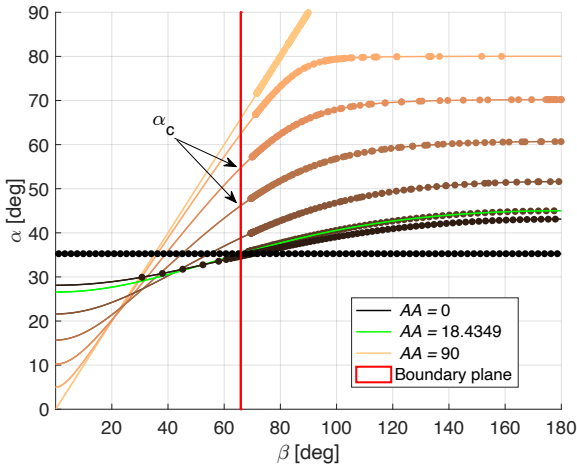

Fig. 9. Cone angle of U as a function of the inner angle for increasing AA (solid lines) together with the computed controls (solid circular markers).

3) *Solar Sail* $(AA_c < AA \leq 90$ deg) regime: The control cannot access the whole set of admissible controls U and keeps to the region delimited by the boundary plane. Although the control no longer reaches the boundary plane, we can use the boundary plane to set a practical limit for the minimum admissible cone angle and define the concept of cone angle bands. The cone angle bands are cone angle intervals that effectively constrain the set of admissible controls U. For $AA < AA_c$, the cone angle band is that of U. For $AA > AA_c$, the upper limit is still that of U, whereas the lower limit is set by the critical cone angle α_c, which is computed as the intersection of the boundary plane with U (see Fig. 9).

Fig. 10 shows the cone angle bands obtained geometrically from U for each AA (solid lines) together with the min/max cone angles of the optimal control computed with GPOPS-II. Note the clear behavioural change at AA_c. The minimum cone angle of the optimal control suddenly jumps to lie within the cone angle band, and remains there from $AA = AA_c$ until $AA = 90$ deg.
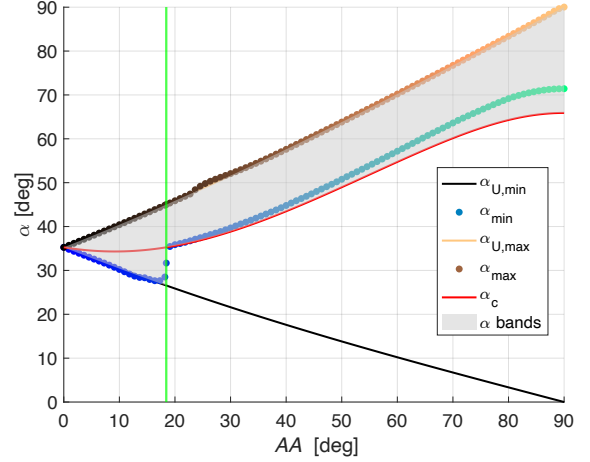

Fig. 10. Cone angle bands together with the minimum and maximum cone angle of the computed optimal controls.

V. OUTLOOK

The results in this paper can be used to initialise a many-revolution optimisation problem and assess the feasibility of a real solar-sail mission scenario. Consider, for example, a multi-revolution C2C transfer from GEO $(AA = 90$ deg) to an orbit 300 km higher with a sail with $\sigma = 0.18$ kg/m^2 (i.e., $a_0 = 0.05$ mm/s^2). Following the procedure in Section III for $AA = 90$ deg, we obtain a performance of $\delta r = 2$ km/rev, which in turn can be used to obtain a rough estimate of the number of revolutions required to gain 300 km in altitude: $\Delta r/\delta r = 300/2 = 150$ rev. A possible approach for solving the optimisation problem would be to build an initial guess as a sequence of one-revolution transfers and then use that guess to initialise a global optimisation algorithm for a refined solution. For a 150 revolutions transfer, the computational cost for optimising 150 one-revolution transfers could be a limiting factor, but by using the results in Fig. 10, the computation of this initial guess can be enhanced by adopting the reduced set U (i.e., the smaller the search space the faster the convergence). We know that the aspect angle of a GEO orbit ranges from 66.6 deg to 90 deg. Fig. 10 indicates that the cone angle band that covers that range is $[58, 90]$ deg, which is a non-negligible reduction of the set of feasible controls. Future work will aim at validating this hypothetical approach to see if it can indeed be generalised to multi-revolution global solar-sail trajectory optimisation

problems.

Secondly, it is interesting to mention that the cone angle bands can be used to assess the feasibility of a real solar sail mission. High-fidelity solar sail acceleration models teach us that, at large cone angles, the solar sail acceleration is difficult to predict and control [1]. C2C transfers requiring large cone angles might therefore not be feasible due to operational constraints. Let us resume our previous GEO example. Near the equinoxes, the cone angle band is as high as $[65, 90]$. It is then reasonable to expect that C2C transfers in the GEO belt will suffer more from cone angle restrictions than, for example, C2C transfers in LEO, where the orbit aspect angle is not as constrained.

VI. Conclusions

This paper has explored the building block of planet-centred solar sailing: the planar Circular-to-Circular transfer (C2C). The timespan of the C2C transfer is constrained to one orbital period and the performance is defined as the achieved orbital radius increase after that one orbital revolution. It was shown that the performance is a function of the ratio of the sail characteristic acceleration and the local gravity. This relationship can be used to compute the C2C performance for over a wide range of mission scenarios around any planet.

In addition, the relationship between the performance and the illumination conditions of the orbital plane was established. The angle between the orbital angular momentum and the incoming sunlight, referred to as the aspect angle (AA), strongly influences the C2C performance, which decreases for increasing AA. Maximum and minimum performances are achieved for $AA = 0$ deg (i.e., orbit perpendicular to the incoming sunlight) and $AA = 90$ deg (orbit parallel to the incoming sunlight), respectively. Performance at $AA = 90$ deg is 20 times worse than at $AA = 0$ deg. Thus, efficient transfer designs should try to avoid high AA.

When the orbit is (near-)perpendicular to the incoming sunlight (i.e., $AA = 0$ deg), the solar-sail C2C transfer closely resembles the same transfer but executed with a low-thrust ion drive. This similarity diffuses with increasing AA. There is a critical value of the AA, coined the critical aspect angle (AA_c), for which the control abruptly changes behaviour. It was found that for $AA > AA_c$, the set of accessible controls (i.e., the domain of the control variables) can be considerably reduced, possibly saving significant computational time in future more refined many-revolution trajectory optimisations.

VII. Acknowledgements

VIII. References

[1] C. R. McInnes, Solar sailing: technology, dynamics and mission applications, Springer Science & Business Media, 2004.

[2] C. G. Sauer Jr., "Optimum solar-sail interplanetary trajectories," in *Astrodynamics Conference*, San Diego, 1976.

[3] J. C. Van der Ha, "The attainability of the heavenly bodies with the aid of a solar sail," *Deutsche Gesellschaft fuer Luft-und Raumfahrt and American Astronautical Society,* vol. 80, no. 3, 1980.

[4] M. Macdonald and C. R. McInnes, "Analytical Control Laws for Planet-Centered Solar Sailing," *Journal of Guidance, Control, and Dynamics,* vol. 28, p. 1038–1048, September 2005.

[5] K. Oguri, G. Lantoine, A. E. Petropoulos and J. W. McMahon, "Solar Sailing Q-Law for Planetocentric, Many-Revolution Sail Orbit Transfers," *Journal of Guidance, Control, and Dynamics,* vol. 46, no. 10, pp. 2005-2014, 2023.

[6] M. Macdonald and C. R. McInnes, "Realistic Earth Escape Strategies for Solar Sailing," *Journal of Guidance, Control, and Dynamics,* vol. 28, p. 315–323, March 2005.

[7] L. Carzana, P. Visser and J. Heiligers, "Locally optimal control laws for Earth-bound solar sailing with atmospheric drag," *Aerospace Science and Technology,* vol. 127, no. 8, p. 107666, 2022.

[8] P. Kelly and R. Bevilacqua, "Geostationary debris mitigation using minimum time solar sail trajectories with eclipse constraints," *Optimal Control Applications and Methods,* vol. 42, p. 279–304, September 2020.

[9] L. L. Sackett, "Optimal solar sail planetocentric trajectories," 1977.

[10] M. A. Patterson and A. V. Rao, "GPOPS-II: A MATLAB Software for Solving Multiple-Phase Optimal Control Problems Using hp-Adaptive Gaussian Quadrature Collocation Methods and Sparse Nonlinear Programming," *ACM Transactions on Mathematical Software,* vol. 41, p. 1:1–1:37, October 2014.